Superposition of Interface and Volume Type Resistive Switching in perovskite nanoionic devices

Sarunas Bagdzevicius[*†], Michel Boudard[†], José Manuel Caicedo[‡], Laetitia Rapenne[†], Xavier Mescot[§], Raquel Rodríguez-Lamas[†‡], Florence Robaut[⊥], Jose Santiso[‡] and Monica Burriel*[*†]*

[†]Univ. Grenoble Alpes, CNRS, Grenoble INP*, LMGP, F-38000 Grenoble, France

* Institute of Engineering Univ. Grenoble Alpes

[§]Univ. Grenoble Alpes, Univ. Savoie Mont Blanc, CNRS, Grenoble INP*, IMEP-LAHC, F-38000 Grenoble, France

[‡]Catalan Institute of Nanoscience and Nanotechnology (ICN2), CSIC and Barcelona Institute of Science and Technology (BIST), Campus UAB, Bellaterra, 08193 Barcelona, Spain

[⊥]Univ. Grenoble Alpes, Grenoble INP*, SIMAP, F-38000 Grenoble, France

*e-mails: sarunas.bagdzevicius@gmail.com; monica.burriel@grenoble-inp.fr

KEYWORDS

Bipolar resistive switching, layered perovskites, interface mechanism, valence change memories, nanoionic devices.

ABSTRACT

The microelectronics industry is currently searching for reliable redox-based resistive switching memories which are filament-free, scale with the electrode size and do not require a high voltage electroforming step. Interface and volume type switching devices are the most promising memristors to achieve these challenging requirements, both for ReRAM (Resistive Random Access Memories) non-volatile memory and neuromorphic computing applications. Here resistive switching (RS) was investigated for the first time in the nanoionic memristors based on $GdBaCo_2O_{5+\delta}$ (GBCO), an oxide with high oxygen mobility. Non-volatile reproducible RS was obtained when GBCO is sandwiched between Ag and $LaNiO_3$ electrodes. The observed bipolar RS could be successfully induced both by voltage sweeps and by pulses, showing asymmetric clock-wise hysteretic R(V) characteristics at room temperature. The temperature dependence of two independent devices in high and low resistance states (HRS and LRS) revealed a gradual decrease of the resistance difference between the two states on cooling from room temperature to 150 K and its increase below 100 K. Similarly, the R(V) switching curves obtained at low temperature showed the disappearance of the hysteresis at 150 K and its reappearance at lower temperatures. The superposition of volume and interface type resistive switching mechanisms have proven to be responsible for the observed non-volatile change of the remnant resistance. The volume-type RS was related to the variation of the GBCO resistivity due to a change in oxygen content. The interface-type RS, on the other hand, was associated to the created electronic and ionic conduction barrier.

The miniaturization of semiconductor Si-based transistors, as well as price reduction and increased functionality in the microprocessors[1] have been the driving force of modern microelectronics and current computation, telecommunication and imaging technologies. However, the physical limits of miniaturization have almost been reached for ordinary planar Si metal-oxide-semiconductor field-effect transistors (MOSFETs).[2] Integrated circuits size scaling is no more physically nor economically feasible. Research in resistive switching (RS) recently exploded as it was established as one of the promising pathways for the so-called "Beyond CMOS" (Complementary Metal–Oxide–Semiconductor) micro- and nanoelectronic memories. The simple yet scalable and stackable two terminal configuration used for ReRAMs (Resistive Random Access Memories) is a promising architecture for future non-volatile memories.[2] ReRAM possess an attractive combination of high information storage density[3] and high operation energy efficiency[4] (0.1 – 3 pJ/bit). The cell area for ReRAM scales down to $4F^2$, where $F < 5$ nm in bipolar filamentary cells, representing the smallest feature size in the lithography process. ReRAMs showing the best performance to date are based on filamentary type mechanisms and typically use oxygen deficient binary oxides, such as HfO_x, as the switching material.[5] Although promising memory characteristics have been achieved in filamentary type redox based memristive memories there are major shortcomings for these devices such as the need of a high voltage forming step and the stochastic nature of the filamentary switching, which leads to a lack of reproducibility and to abrupt SET and RESET transitions hindering applications in multilevel memories and analog-like neuromorphic computing.[6] Thus the industry has now moved its focus to forming-free devices which need less than 2 V for all their operations and which present area-scaling of the current. In other words, filaments must be avoided, and interface or volume type switching has become of major scientific and industrial interest.

Hence there is now a need to find new memristive materials and, more importantly, to understand and control the change in the interfacial electronic properties when applying an electric field to the device, which can lead to several processes including the movement of oxygen ionic carriers, valence-change reactions, trapping of charge carriers and interfacial Mott transitions [7].Contrary to binary oxide based resistive switching devices, non-filamentary oxide valence change memristors do not suffer from stochastic switching nature[7] and have the advantage of multilevel storage[8] and continuous (interface or volume type) switching, a very important characteristic for their application in synaptic electronics.[9] Interface/volume type RS is usually observed in electrode/perovskite/electrode structures, [7, 10] e.g. electrode = metal or semiconductor.

Intrinsic or artificially engineered materials showing metal-insulator transition (MIT) have a huge potential as nanoscale switches[11]. Various materials exhibiting MIT (e.g. Mott-Hubbard type as $(V_{1-x}Cr_x)_2O_3$[12], $Pr_{0.7}Ca_{0.3}MnO_3$[13] or charge-transfer type[14] as $NdNiO_3$ and $YBa_2Cu_3O_{7-\delta}$) have also been examined for memristive applications. Particularly interesting is the reversible modulation of the nonvolatile superconducting−insulator volume phase transition in epitaxial $YBa_2Cu_3O_{7-\delta}$ films by electric manipulation[15]. By using multielectrode patterned devices with silver electrodes Palau *et al.* demonstrated that both the normal state resistance and the superconducting critical temperature can be reversibly manipulated in confined active volumes by electrochemical oxygen doping.

Other recent works have focused in the use of materials with high ionic conductivity, such as ceria and zirconia-based oxides, for the design of memristive devices. These oxide layers can adopt different functionalities either as main switching material or as functional layers within multilayer memristive heterostructures. On the one hand, by studying the gadolinia-doped ceria solid solution in $Pt/Ce_{1-x}Gd_xO_{2-y}/Pt$ devices[16] Schmitt *et al.* demonstrated that the resistive switching response

can be tuned by the configuration of its oxygen vacancy defects and their mobility. On the other hand Ortega-Hernandez *et al.*[17] showed that the insertion of a CeO_{2-x} layer on top of a perovskite $La_{0.8}Sr_{0.2}MnO_3$ memristive films results in smaller SET/RESET operation voltages and in a substantial enhancement of the resistance ratio. This deep modification of the resistive switching characteristics was attributed to the functional role of CeO_{2-x} as oxygen reservoir, promoting the migration of oxygen between the two layers. Yttria-stabilized zirconia (YSZ) also presents very promising switching characteristics (large resistance window of 10^5 and possibility of obtaining reversible multilevel resistance states) when sandwiched in Pt/YSZ/Nb:$SrTiO_3$ heterostructures[18], showing potential application in multilevel nonvolatile memory devices. In this case the resistive switching is attributed to the modulation of the YSZ/Nb:$SrTiO_3$ Schottky-like junction depletion at the interface. YSZ can also be used as tunnel barrier in $Pr_{0.48}Ca_{0.52}MnO_3$ (PCMO) perovskite memristive heterostructures[19], where an exchange of oxygen ions between PCMO and YSZ causes an electrostatic modulation of the effective height of the YSZ tunnel barrier and is thereby the underlying mechanism for resistive switching in these devices.

$GdBaCo_2O_{5+\delta}$ (GBCO) double perovskite is a fascinating material with a rich phase diagram over a wide oxygen stoichiometry and temperature range, including a metal-insulator transition at low temperature[20] and fast oxygen diffusion at high temperatures[21]. The motivation of this work is to combine the mixed ionic and electronic transport properties of GBCO and use this perovskite oxide to build memristive nanoionic devices in which different physical properties can be accessed by continuously doping CoO_2 planes with either electrons or holes by simply changing its oxygen content.

Here we report on novel nanoionic perovskite heterostructures (Ag/GBCO/$LaNiO_3$) as RS memories. We show the structural and electrical characterization results and draw a possible

scenario (oxygen stoichiometry dependent MIT and creation of a bipolar p-n junction) to explain the bipolar RS and continuous change observed in the device resistance. Oxygen drift and diffusion, together with the semiconducting nature of the transport in the heterostructure allows for the creation of conduction barriers at the electrode-oxide interfaces. We will show how the interplay between the created barriers, depletion regions, and redox mediated change in oxygen stoichiometry leads to a non-volatile change in the device resistance.

EXPERIMENTAL

Material and device fabrication. LaNiO3 bottom electrode (20–61 nm) and GdBaCo2O5+d epitaxial thin films (8–31 nm thickness) were deposited by PLD (pulsed laser deposition) using a KrF excimer laser (repetition rate 10 Hz; fluence 1.1 J cm 2) at 700 1C substrate temperature and at an oxygen partial pressure of 60 mTorr. The deposition temperature was kept at 700 1C to avoid the decomposition of the LaNiO3 electrode. Ceramic targets were used for both GdBaCo2O5+d (with 5 wt% excess of Co) and LaNiO3 (stoichiometric). Under these deposition conditions GBCO showed a 2D island-coalescence growth mode. Thememristive nanoionic devices were completed by depositing 200 nm thick Pt and Ag metal top electrodes using an e-beam evaporation system after a gentle (20 s) Ar plasma cleaning procedure. The device geometry was defined by UV photo- and laser-lithography.

Electrical measurements. Electrical characterization was carried out using the following instruments at ambient conditions: DC current–voltage I(V) characteristics were measured using an Agilent B1500 semiconductor parameter analyser and triaxial cables for low current measurements. AC impedance was measured using an HP 4280A LCR analyser with coaxial cabling and open/short calibration procedure. Temperature-dependant I(V) sweeps were measured

using Keithley 2428 electrometers under low vacuum. The temperature was changed using a closed cycle He cryostat and controlled/stabilized by a LakeShore 331 controller. The voltage was always applied to the top Ag electrode, while the bottom LNO/GBCO/Pt electrode was grounded. RS was achieved without the need of a forming step. A 100 mA current compliance (not reached in normal device

operation) was used during the voltage sweeps and pulses. The I(V) characterization was carried out in the stationary regime to avoid transient currents due to charging capacitances in the circuit. A 20 ms integration time was used for the voltage sweeps (with 10 mV steps) and 2 s for the write and 40 ms for the read voltage pulses in the RHSL mode. For the low temperature measurements, the formation of ice by the atmospheric humidity was prevented by using low vacuum conditions in the measurement chamber.

Structural and microstructural characterization. The structure and strain in the thin films were determined by X-ray diffraction on a high-resolution triple-axis diffractometer (D8 Discover, Bruker) using a monochromatic Cu Ka (filtered Cu Kb wavelength radiation) radiation source and position sensitive detector. Using different scan possibilities (Y–2Y, rocking curve o, reciprocal space maps (hkl)) the layers thickness, lattice constants, crystallographic orientation, and quality of thin films were examined. TEM and HRTEM images were obtained with a JEOL JEM 2010 LaB6 microscope operating at 200 kV with a 0.19 nm pointto-point resolution. EDX mapping was collected by STEM with a JEOL 2100F FEG microscope operating at 200 kV with a 0.2 nm resolution in the scanning mode and equipped with a JEOL SDD Centurio detector with a large solid angle of up to 0.98 sr. Scanning electron microscopy images were taken on a FEI Quanta 250 ESEM FEG with 1–30 kV Schottky field emission gun. TEM lamellas were prepared with a double column FIBSEM microscope according to the lift-out method. The equipment used was a ZEISS

NVision 40 equipped with a gallium ion source operating at a maximum accelerating voltage of 30 kV, a carbon and platinum gas injection system and a Kleindiek micromanipulator.

RESULTS AND DISCUSSION

Device fabrication and structural characterization. For the design of the memristive device, we selected $GdBaCo_2O_{5+\delta}$ as the main active material. This double-perovskite has an intrinsic MIT[20] close to room temperature for $\delta = 0.5$. In addition, by changing its oxygen content it can be transformed into a nanoscale insulator/conductor mixture by controlled hole or electron doping.

Figure 1 shows the X-ray diffraction pattern of the GBCO/LNO//STO (GBCO = $GdBaCo_2O_{5+\delta}$, LNO = $LaNiO_3$ and STO = $SrTiO_3$) heteroepitaxial thin films (31 nm for GBCO and 61 nm for LNO measured by TEM) grown on a $SrTiO_3(001)$ substrate and with top Pt and Ag metal electrodes. The deposition conditions to obtain the layered "112" (Gd:Ba:Co ratio 1:1:2) perovskite[21] had been previously optimized for its application as intermediate temperature solid oxide fuel cell (SOFC) cathode [22,23] in views of its good mixed ionic and electronic transport properties. Double perovskite films with the c-axis aligned out of plane were obtained by growing the films at 850ºC. Nevertheless, in this work a lower deposition temperature of 700ºC was selected to maintain the LNO layer's microstructure, as at higher deposition temperatures LNO started decomposing and NiO crystals appeared at the film surface. Figure S1 shows the Secondary Electron Microscopy (SEM) and Atomic Force Microscopy (AFM) images of the epitaxial LNO and GBCO films obtained.

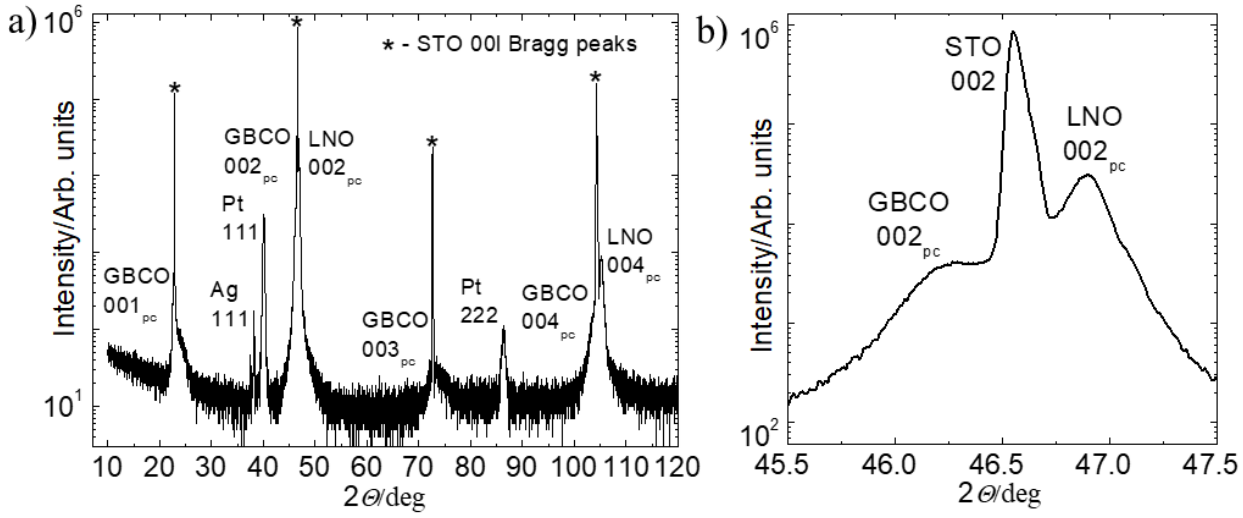

Figure 1. X-ray diffraction pattern of the $GdBaCo_2O_{5+\delta}/LaNiO_3//SrTiO_3$ heterostructure using a $Cu_{K\alpha_1}$ X-ray source. a) Epitaxial GBCO and LNO layers in which only the 00l Bragg peaks (l = integer, pseudocubic cell) are observed. Ag and Pt diffraction peaks are from the top electrodes. b) Enlarged area close to STO 002 Bragg peak. $GdBaCo_2O_{5+\delta}$ = GBCO, $LaNiO_3$ = LNO and $SrTiO_3$ = STO.

The $\delta = 0.5$ $GdBaCo_2O_{5+\delta}$ bulk parent compound has an orthorhombic Pmmm Z = 2 structure[24] at standard conditions with a = 3.878 Å, b = 7.831 (b/2 = 0.39155 nm) Å and c = 7.535 Å (c/2 = 0.37675 nm) lattice parameters.[25] In Zapata *et al.*[21] the authors showed that GBCO grows with the c-axis out-of-plane oriented when deposited directly on a $SrTiO_3$(001) substrate and a-axis out-of-plane when deposited on $NdGaO_3$(110) substrates. This is due to the minimization of the in-plane epitaxial strain at the deposition temperature, as the $NdGaO_3$ pseudocubic in-plane lattice parameters (0.3864 nm and 0.3855 nm) are smaller than the cell parameter for $SrTiO_3$ (0.3905 nm). In Figure 1a the Bragg diffraction peaks correspond to a simple pseudocubic perovskite cell with integer Miller indices; no cell doubling was observed. The calculated GBCO out-of-plane lattice parameter (from the most intense Bragg diffraction peak, Figure 1b) of 0.3928 nm is close

to the bulk b/2 = 0.39155 nm value. The absence of half order diffraction peaks typical for the c-axis doubling means that in our heterostructure either GBCO is oriented with the b-axis out of plane with very short correlation length domains, or it does not form an out-of-plane aligned (c axis) double perovskite at this compromise deposition temperature (700 ºC). The calculated out-of-plane LNO lattice parameter is a_{pc} = 0.3878 nm is larger than bulk LNO (a_{pc} = 0.384 nm) but smaller than STO (a = 0.3905 nm) and indicates that the tensile strain in the 60 nm LNO layer is partially relaxed by forming defects. The effective lattice parameter of the relaxed LNO is smaller than that of the single-crystal STO and thus induces the growth of the c-axis in-plane oriented GBCO. The increase of the out-of-plane LNO lattice parameter is likely due to stacking faults which had already been reported in the literature for epitaxial $LaNiO_3$ films[26]. A defective LNO layer and the single-perovskite domains in GBCO are confirmed by the TEM images and selected area electron diffraction patterns (SAED) shown in Figure 2.

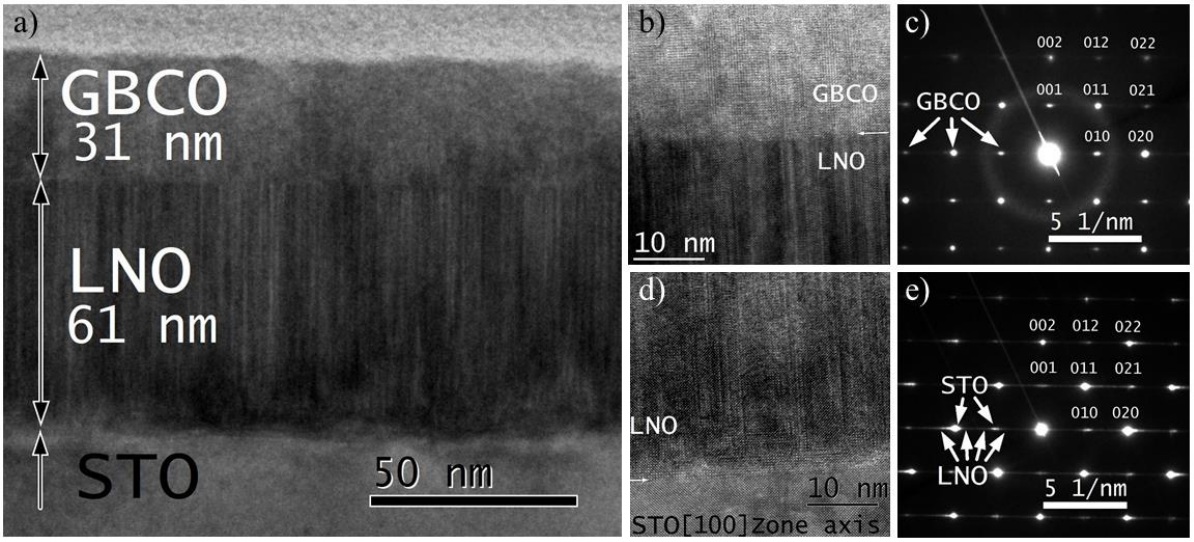

Figure 2. a) Bright field TEM cross-section of the $GdBaCo_2O_{5+\delta}/LaNiO_3//SrTiO_3$ heterostructure. HRTEM in b) shows the LNO and GBCO interface. Selected area electron diffraction pattern (SAED) of LNO/GBCO layers in c) and of STO//LNO layers in e). Only the diffraction peaks corresponding to simple cubic (or pseudocubic) lattices (no superlattice peaks) with a cube on cube

epitaxial relation appear. HRTEM in d) displays a perfect epitaxy of the LNO layer in the first few bottom nanometers (an arrow indicates the sharp STO//LNO interface).

The bright field TEM cross-section image in Figure 2a with the [100] zone axis shows continuous epitaxial films with vertical stripe contrast aligned perpendicular to the substrate for the LNO layer. The HRTEM image (Figure 2d) shows that for the first few nanometers LNO grows fully coherent to the STO substrate. Then, elastic strain builds up and induces relaxation by the formation of stacking faults (Figure S2) with a shift of ½ unit cell along the vertical direction and one NiO_2 plane missing at the defect boundary. A high number of defects are aligned in the out-of-plane direction and induce a streaky contrast along the [010] direction of the SAED pattern (Figure 2e). As shown in the GBCO HRTEM image (Figure 2b), only certain vertical defects in $LaNiO_3$ transfer to the GBCO film. The use of an LNO template film and a deposition temperature of 700 ºC prevents GBCO from developing a fully ordered layered perovskite structure (out-of-plane). No cell doubling is observed by SAED in GBCO (Figure 2c) indicating the existence of either a single perovskite phase or that the ab-plane is oriented perpendicular to the zone axis of the tetragonal perovskite.

Electrical measurements and resistive switching characterization. The complete electrical characterization of the devices schematically depicted in Figure 3a was carried out. Pairs of the devices were fabricated on the same substrate (Ag/GBCO/LNO and LNO/GBCO/Pt) in back-to-back configuration. The LNO/GBCO/Pt heterostructure always showed a low (120-140 Ω) and linear resistance and was considered as an ohmic contact to the lower LNO electrode. The measured resistance of two LNO/GBCO/Pt heterostructures in series scaled with the LNO layer length as a geometrical resistance and no change in resistance due to the applied voltage was ever

observed. Thus, henceforth we analyze only the Ag/GBCO/LNO device and treat LNO/GBCO/Pt as a series resistance.

Prior to the RS measurements, the electrical properties of individual GBCO films and LNO films deposited directly on to STO (001) substrates was investigated. Hall and Van der Pauw measurements were carried out on a 70 nm thick GBCO film for which Ag electrodes were hand-painted. The effective Hall coefficient measured was negative R_H = -0.4402 m^3/C, indicating that the main contribution came from negatively charged carriers (electrons). The room temperature resistivity value measured of 94.16 mΩ·cm is in good agreement with literature values for insulating GBCO bulk with δ close to 0.5.[20]

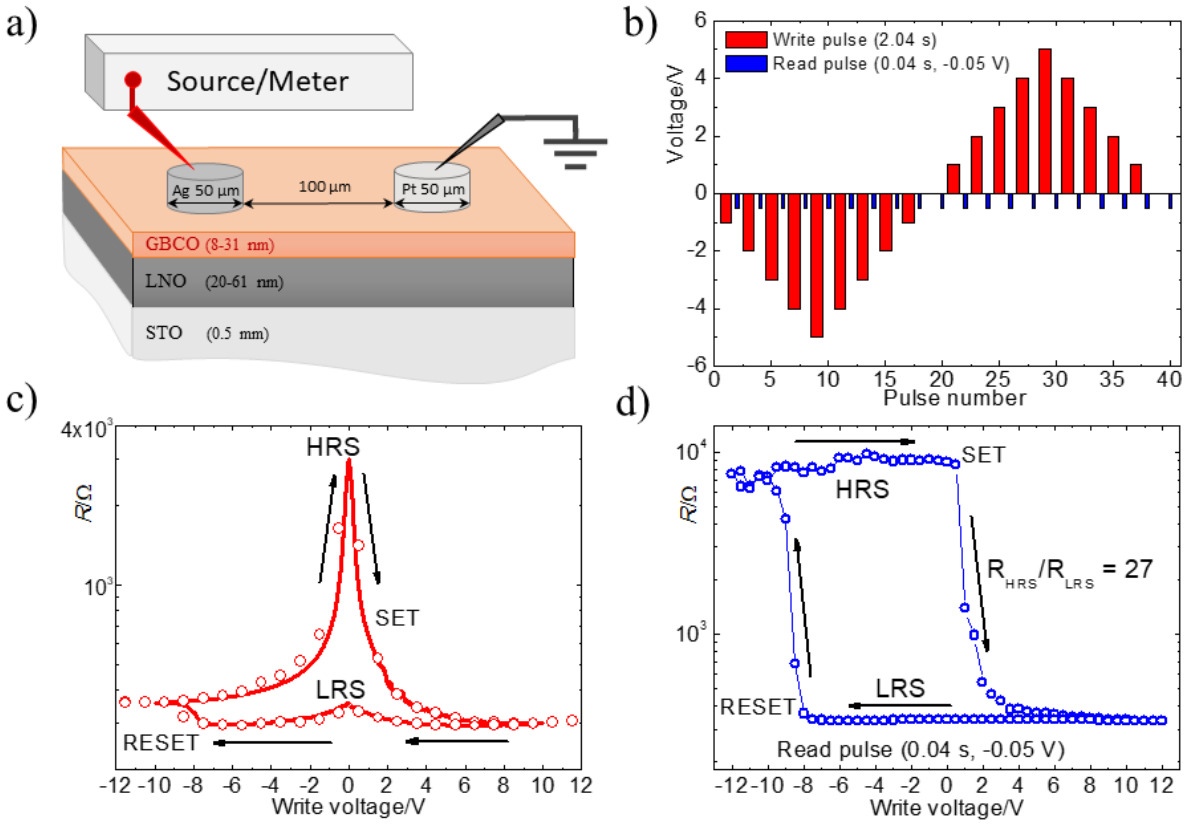

Figure 3. RS measured on a $GdBaCo_2O_{5+\delta}$/ $LaNiO_3$// $SrTiO_3$ (GBCO = $GdBaCo_2O_{5+\delta}$, LNO = $LaNiO_3$ and STO = $SrTiO_3$) heterostructure in voltage sweep and resistance hysteresis switching loop (RHSL) modes. a) Sketch of the device (not to scale) used for the electrical measurements.

b) RHSL scheme, c) instantaneous resistance during voltage sweep (red line) and write pulses (red circles), d) remnant resistance measured with read pulses at -50 mV after each write pulse (line serves as a guide for the eyes).

The overall conductivity of the LNO thin films (ρ = 120 - 170 $\mu\Omega\cdot$cm) is very close to the value reported in the literature for single crystal quality epitaxial thin films 10-30 nm thick (ρ = 150 $\mu\Omega\cdot$cm)[27]. The metallic $LaNiO_3$ phase is thus percolating throughout the sample and the observed vertical defects (stacking faults or additional LaO planes[28]) do not affect the overall conductivity.

The pulse scheme used for resistance hysteresis switching loop (RHSL) measurements is shown in Figure 3b. The corresponding instantaneous R(V) curves present a characteristic "sombrero" symmetrical shape as shown in Figure 3c. Both sweep and pulse measurements show a very good match; a clockwise hysteretic R(V) switching occurs from low resistance (LRS, the "ON" state) to high resistance state (HRS, the "OFF" state).

A gradual SET transition is triggered when a positive bias (applied to the top Ag electrode) reaches a characteristic voltage range (typically between +0.5 V to +3 V). A RESET transition (from LRS to HRS state) occurs when the negative bias reaches the characteristic voltage (-6 V to -8 V range). The RESET transition occurs in a range of less than 1 V. The SET transition, on the other hand, is gradual and occurs over a range of a few volts (Figure 3c), suggesting multiple transitions and several intermediate resistance states.

The narrow voltage range for the RESET transition is due to the small drop of applied external voltage (V_{ext}) in the GBCO film ($R_{GBCO} < R_{LNO}$ in LRS) before the negative switching voltage is reached (-8 V in Figure 3c). When $V_{ext.}$ surpasses the negative switching voltage ($V_{ext.} < -8$ V) a self-reinforcing switching sequence is triggered: the larger the volume of GBCO film switched from LRS to HRS, the larger the $V_{ext.}$ drop in the GBCO film (compared to the LNO electrode),

leading to the fast conversion of the GBCO film to HRS ($R_{GBCO} > R_{LNO}$ in HRS). The same reasoning applied to the SET transition explains the gradual and asymmetric change in resistance when switching from the HRS to the LRS. Initially at HRS almost all the $V_{ext.}$ drop (positive) occurs across the GBCO layer. Above a certain positive switching voltage ($V_{ext.} > +1.5$ V in Figure 3c) the resistance of the GBCO layer sharply decreases resulting in a smaller V_{ext} drop in the GBCO layer compared to the lower electrode (again $R_{GBCO} < R_{LNO}$), leading to the observed gradual increase of positive switching potential to complete the HRS to LRS transition. The highly nonlinear R(V) behavior at small voltages (from -1 V to +1 V in Figure 3c),.as will be demonstrated subsequently, is precisely the one responsible for the high memory window observed ($R_{HRS}/R_{LRS} = 27$ in Figure 3d). R_{HRS}/R_{LRS} is defined as the resistance ratio between the two stable resistance states, i.e. in the voltage range from -2 V to +1 V measured at -50 mV read voltage (Figure 3d).

It should be pointed out that immediately after fabrication the device was already in LRS. This fact, together with the STEM-EDX observations (Figure S3) in which no silver migration was detected after device operation in the GBCO film under a switched Ag electrode, rules out the possibility of Ag electromigration as the mechanism responsible for resistive switching in these devices. All the devices tested could be cycled between the HRS and LRS after an initialization step, despite some differences in the initial resistance of the devices, which depends on their history. This initialization step consisted of several full voltage sweeps (0 V to -10 V, to 0 V, to +10 V and back to 0 V) to bring the device to LRS. The devices which were already in LRS (immediately after fabrication) did not require the initialization step.

We have characterized the GBCO-based memristive nanoionic devices in the pulsed voltage mode measuring both the instantaneous and remnant resistance. A representative square hysteresis

switching loop (RHSL) is shown in Figure 3d, where the remnant resistance is plotted as a function of the externally applied voltage. A reproducible resistance R_{HRS}/R_{LRS} ratio of 27 was obtained when cycling the full voltage range necessary to reversely switch from LRS to HRS (±12 V).

Interface and volume type switching mechanisms typically present area-dependent resistance for both the LRS and HRS[7]. We have probed the area scaling for these memristive devices using different top electrodes circles with diameters spanning from 20 to 70 µm. The resistance scaling obtained is displayed in Figure 4a. The values displayed in Figure 4a are obtained from the RSHL close to 0 V write voltage and measured with a -50 mV read voltage. For the whole range of electrode sizes, we were able to obtain reproducible resistive switching both in sweep and RHSL modes (representative curves shown in Figure 4b).

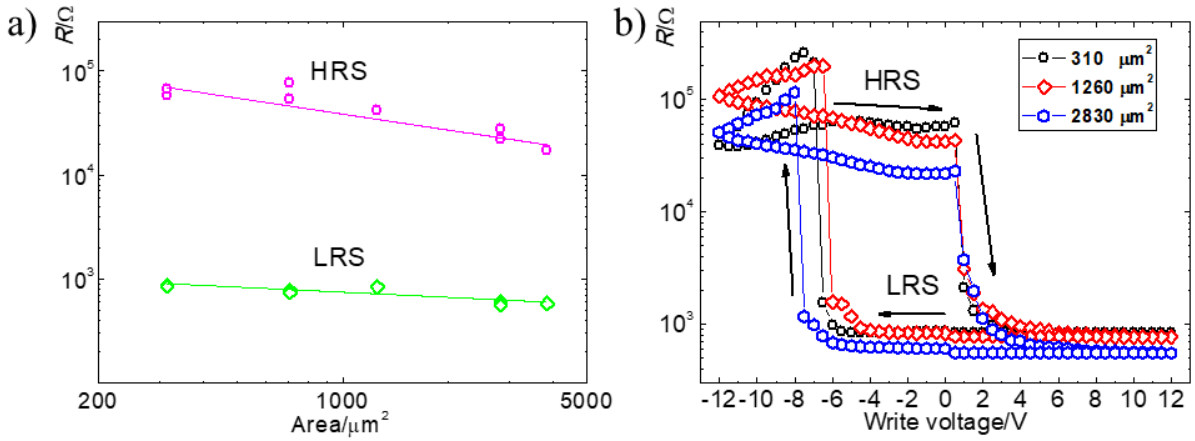

Figure 4. Area-scaling of the HRS and LRS in the GBCO heterostructure. a) Resistance in the LRS (green diamonds) and in the HRS (pink circles). The lines are linear fits to the experimental data. b) Shows the RHSLs for different Ag electrode sizes (lines serve as a guide for the eyes). 20 to 70 µm diameter top Ag and 50 µm diameter counter Pt electrodes, 20 nm LNO and 8 nm GBCO layer thicknesses, the distance between the Ag and Pt top electrodes was approximately 100 µm.

While the HRS clearly shows area scaling, the LRS is less sensitive to the top electrode size. Nevertheless, a small decrease cannot be discarded (30% ΔR resistance difference). The small area

dependence of the LRS suggests metallic conduction through the Ag/GBCO/LNO heterostructure, for which a change in the geometrical resistance is too small to be observed for the relatively small differences in electrode size measured. All RHSLs are asymmetric, shifted to the negative potential side. The SET and RESET switching voltages do not depend on the electrode area (less than 2 V variability for the RESET transition) indicating a SET and RESET transition dependence on the current density, shown in Figure 4b. Due to the area scaling of the HRS (geometrical resistance decrease with electrode area increase), the resistance ratio also increases by decreasing the top electrode area, resulting in a memory window of around 100 for a 20 μm diameter top Ag electrode.

No evidence of cell degradation was observed after 200 cycles switching between the LRS and HRS with opposite potential voltage pulses, as shown in Figure 5a. There is certain variability in the resistance value for both states, which could point towards a multipath switching scenario[29] in which a high number of parallel switching elements are present in the film but do not reach exactly the same factor *f* (fraction of pathways in high resistance) for consecutive voltage pulses. The same tendency is upheld by short-term retention measurements, as shown in Figure 5b, where a small resistance increase with time was observed for both resistance states during the first hour. A continuous increase of the *f* factor in the HRS and a slow back-switch of some of the pathways to high resistance when the device is in LRS, would give rise to the observed initial gradual resistance increase. Nevertheless, the large resistance difference between the two states is maintained during 6 hours of continuous measurement. In addition, different intermediate resistance states were measured when increasing the voltage of the pulses with opposite polarity to switch the cell resistance (Figure S4), opening the possibility to multilevel RS in these devices.

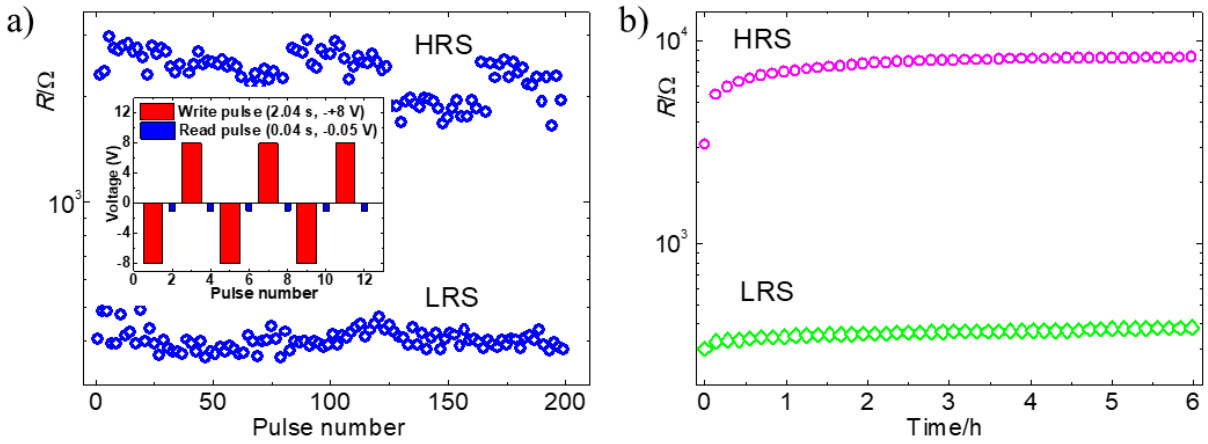

Figure 5. Endurance a) in pulse mode for 200 cycles (inset shows pulse scheme) and retention b) in continuous mode. The memristive heterostructure was switched to HRS by applying a 30 s pulse of -12 V and to LRS by a 30 s pulse of +12 V. The retention was measured continuously applying -50 mV and reading the current for 6 h.

For an in-depth study of the conduction mechanisms separate memristive devices were switched to low and high resistance state at room temperature and then the temperature evolution of the resistance was measured on cooling. Down to 85-100 K the resistance of the HRS and LRS (Figure 6a) follows the temperature dependence of GBCO single crystals reported by Taskin *et al.* [20], in which the authors measured a shift in the resistivity-temperature curves for crystals with different oxygen concentrations. In particular, the HRS state qualitatively follows $\delta \approx 0.5$ GBCO bulk temperature dependence (similar slope measured in the 100-300 K range to the one reported in [20]), while the resistance of the LRS evolves as GBCO with slightly larger oxygen content ($\delta \geq 0.51$)[20] and with a smaller resistance value at room temperature. The GBCO resistance curves approach each other at the same temperature range as reported for $\delta = 0.5$ and $\delta = 0.51$[20].

In the temperature range between 100 K to 150 K no difference in resistance between the two devices is observed. Nevertheless, the difference reappears at temperatures lower than 100 K, as

shown in Figure 6a. For further insight the temperature was stabilized at selected values at which full electrical characterization of the memristors was carried out by RHSLs. Three representative temperatures are shown in Figure 6b. Indeed, no resistive switching was observed at 150 K as the R(V) curve followed eight-wise direction with no remanence at 0 V bias. Such symmetric and hysteretic behavior is conformable with a change in resistance due to the reversible movement of oxygen vacancies in the GBCO layer together with oxygen partially blocking electrodes.

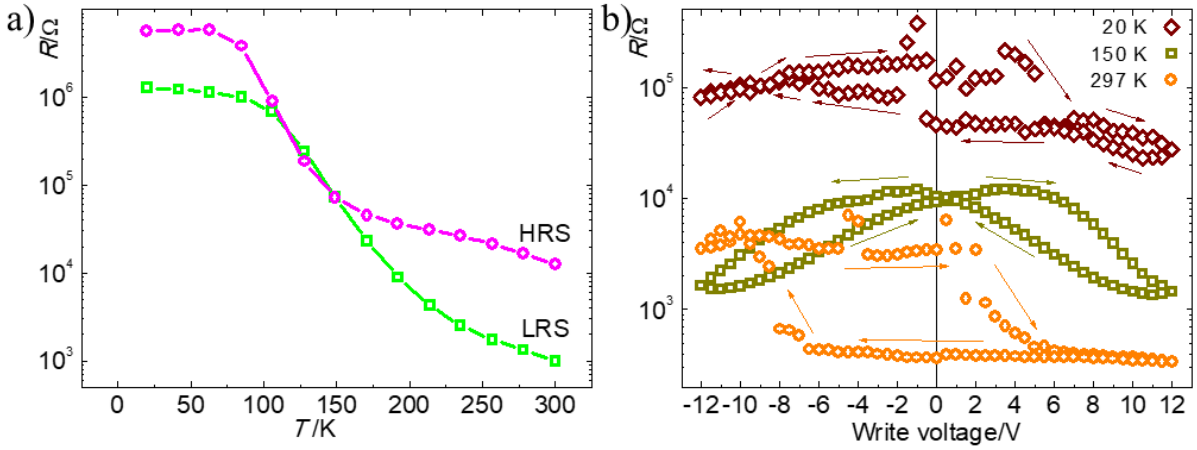

Figure 6. Temperature dependence of the resistance in HRS and LRS on cooling. The memristors resistance was measured with a small negative I(V) sweep a), values shown at -50 mV (the lines are guides for the eyes). Subsequent RHSLs on heating from 20 K to room temperature b). The RS is suppressed in the same region where the resistance of the HRS and LRS becomes equal, and it reappears at lower temperatures.

The resistive switching behavior observed at temperatures below 100 K is in agreement with the superposition of two switching mechanisms, i.e.: non-volatile clockwise R(V) switching, as observed at room temperature, and eight-wise R(V) (crossing at 0 V), as observed at 150 K. The RHSL measured at 20 K shows a similar resistance evolution to the one observed at room

temperature with the hysteresis loop centered at 0 V (-6 V to +6 V bias range), while a small superimposed eight-wise R(V) loop seems to appear below -8 V and above +8 V.

As the LNO lower electrode is metallic, its contribution to the total resistance will decrease and become negligible at low temperatures. The resistivity of GBCO on the other hand increases orders of magnitude at low temperatures. As a result, due to the overall larger resistance of the GBCO layer both in HRS and LRS states, below 100 K the R(V) curve becomes centered at 0 V. Most of the applied external voltage $V_{ext.}$ drops in the GBCO layer, thus making the RESET and SET transitions more symmetric (approximately -6 V for RESET and +6 V for SET transitions at 20 K in Figure 6b).

Three different interfaces are present in these memristive nanoionic devices: Ag/GBCO (metal/semiconductor), GBCO/LNO (two semiconducting oxides which could form bipolar junctions) and GBCO/Pt (semiconductor/metal). Depending on the band alignment these junctions can show rectifying behavior if the conduction barriers are high enough. Electrical bias modulation of the rectifying barriers was accounted as the main bipolar switching mechanism in perovskite oxides in many publications[30, 31]. However, there is no rectifying behavior when the conduction barriers are relatively low, due to the small difference between work functions and electron affinities, or when the Fermi level is pinned at the interface due to the dangling bonds. We have induced resistive switching in the Ag/GBCO/LNO heterostructures and no rectifying behavior was observed neither for the HRS nor for the LRS states.

We have used impedance spectroscopy to extract information about the conduction barriers and discriminate between volume and interface type mechanisms: e.g. Space Charge Limited Current or Poole-Frenkel mechanisms for volume type, and direct tunneling or Schottky barrier modulation for interface type. The low-frequency (20 Hz to 1 MHz) impedance and phase angle measurements

at room temperature are displayed in Figure 7a for both HRS and LRS states and the complex impedance (modulus and phase) bias dependence is shown in Figure 7b.

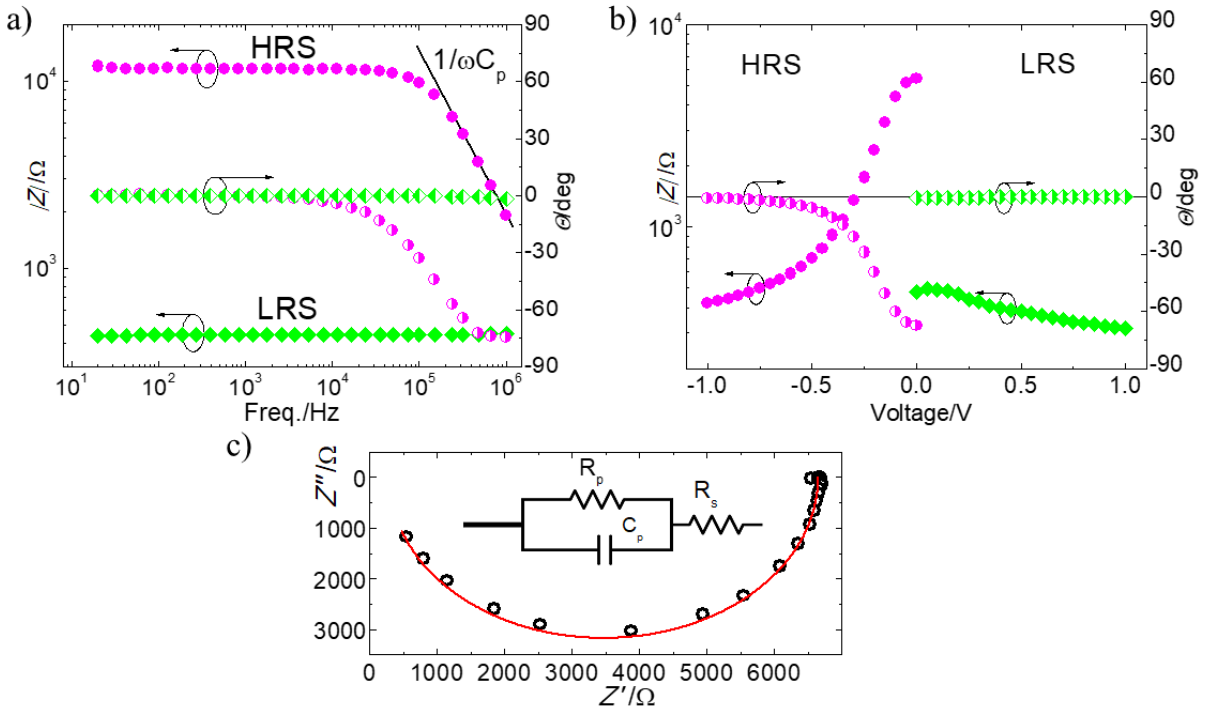

Figure 7. Low-frequency Bode-plot of the impedance a) of the memristive device in LRS (green diamonds) and HRS (purple circles). In the HRS with respect to LRS an additional capacitive element appears in parallel to a pure resistance. b) Modulus and phase of the impedance as a function of the applied voltage at 0.3 MHz. The impedance modulus rapidly decreases at higher negative voltages in the HRS while in the LRS the bias dependence is very small. c) Cole-Cole plot of the memristor in the HRS. The semicircle indicates a Debye-type system with one relaxation time. The experimental data (black circles) were fitted with Equation 1 (red line), corresponding to the capacitor and resistor in parallel with an additional series resistance.

The HRS equivalent circuit (inset in Figure 7c) consists of a capacitive element in series with a pure resistance. The capacitance appears as a linear frequency dependent component (in log-log scale) for both the impedance modulus and the phase angle (Figure 7a), while the obtained negative

phase angle close to -90º indicates a capacitive impedance. On the other hand, there was almost no change in the frequency dependence of the impedance modulus and phase angle when the same device was switched to LRS. As shown in Figure 7b, the HRS complex impedance is bias dependent while in the LRS state the impedance is bias independent. The frequency dependence of the real and imaginary parts of impedance (Z' and Z") was modeled as a resistance in series followed by a resistance and a capacitance in parallel. The equivalent electrical circuit is shown in the inset of Figure 7c. The lumped element model simplification is justified by the small electrical circuit dimensions (the largest dimension is a few hundreds of micrometers) and by the low frequencies involved (< 1 MHz). The following complex equation was used to describe the complex impedance frequency response of the Ag/GBCO/LNO memristor:

$$Z^* = R_s + \frac{R_p}{1+(\omega C_p R_p)^2} + i\frac{\omega C_p R_p^2}{1+(\omega C_p R_p)^2}, \quad (1)$$

where R_s and R_p are the series and parallel resistances respectively, C_p is the parallel capacitance and $\omega = 2\pi f$ the cyclic frequency.

The Cole-Cole plot of the HRS at room temperature displayed in Figure 7c shows a good agreement between the model and the experimental data. A nonlinear least square fit allowed to extract the fitting parameters $C_p = 0.146$ nF, $R_p = 6350$ Ω (very close to the resistance of the device in HRS measured by I(V) sweeps and RHSLs, Figure 3c and d) and $R_s = 300$ Ω (similar to the LNO contribution when device resistance was measured in LRS, Figure 3c and d). Although an even more accurate fit of the experimental data can be obtained by using a constant phase element (CPE) instead of a capacitor, this would hinder a straightforward physical parameters extraction, and consequently has not been carried out.

The obtained capacitance (0.146 nF) when the device was switched to HRS cannot be due to a simple parallel plate capacitor with GBCO insulating phase as a polarizable medium and a parasitic

capacitance from the contacts. Indeed, using the reported dielectric permittivity value of ε' = 13 [32] at infrared frequencies, the calculated distance between the plates (in the parallel plate capacitor formalism) is unphysically small (d = 0.2 nm) and does not coincide with the real device dimension of d = 31 nm. Low-frequency dielectric permittivity values are typically a few times higher due to the sum of several polarization processes (dipolar, ionic and electronic polarization). Up to a twentyfold higher relative permittivity of $\varepsilon_r = 360$ could be justified, as is the case for high-k materials such as $SrTiO_3$ (with ε' = 300 at room temperature). Nevertheless, even a 20 times higher dielectric permittivity would still be too small to account only for the geometrical capacitance. These considerations allow assuming that the measured capacitance is due to a network of parallel capacitors consisting of either a depletion layer[33] formed by semiconducting GBCO and metallic LNO (unipolar Schottky-like junction), or of diffusion capacitances[34] at the bipolar junction between the n-type GBCO (when $\delta < 0.5$)[20] and p-type conducting LNO phase. LNO p-type conductivity has been previously reported for oxygen hyper-stochiometric $La_2NiO_{4+\delta}$ [35] (locally formed by additional LaO planes seen in the Figure 2 and Figure S2) and for the epitaxial ultrathin films of metallic $LaNiO_3$ grown on $SrTiO_3$[36]. The rather high 0.146 nF capacitance value in the forward biased junction is more compatible with the bipolar junction and diffusion capacitance. This conclusion is supported by the impedance observed in the LRS (Figure 7a) which only presents a resistive contribution. For the case of a unipolar Schottky junction there should be a small, but non-zero capacitance when biased with a positive voltage, which is not present in Figure 7b.

The frequency dependence of the complex impedance vs. voltage bias in the HRS is displayed in Figure 8a and b, in which the experimental data were fitted using Equation 1. The series

resistance does not depend on the applied negative voltage, while the parallel resistance and the capacitance show bias-dependence, as displayed in Figure 8c.

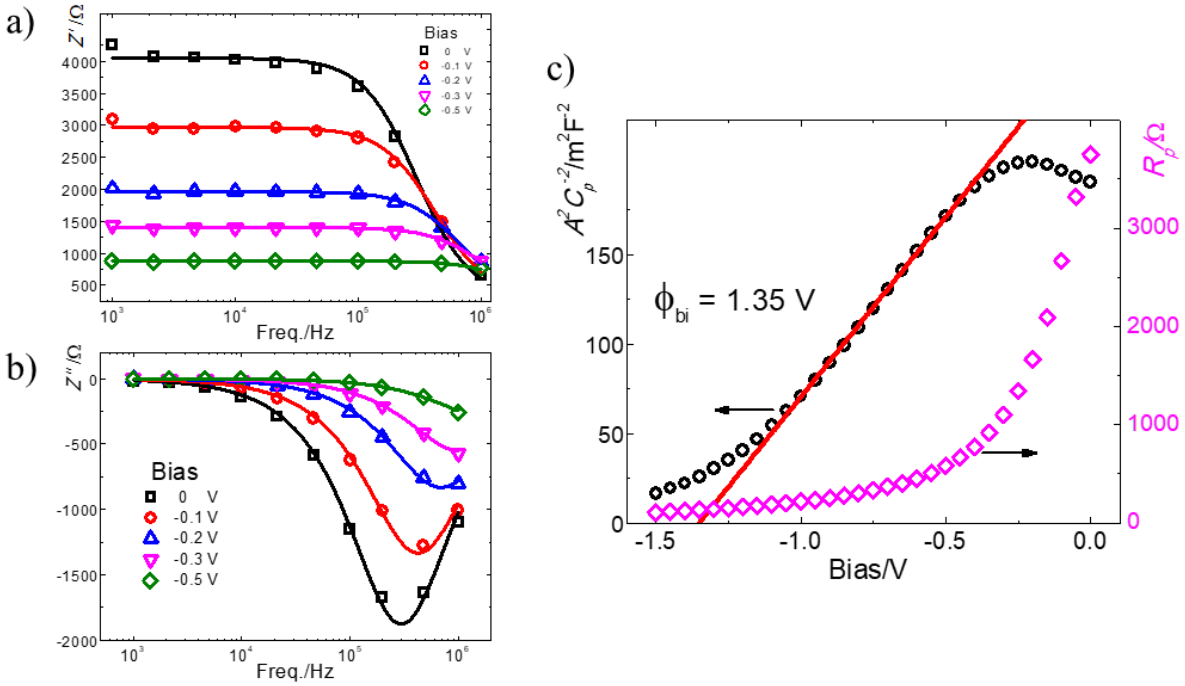

Figure 8. Applied voltage dependence of the real a) and imaginary b) parts of the complex impedance of the HRS (open symbols are experimental data, lines are fits to Equation 1). c) Applied voltage dependence of the inverse capacitance density dependence. The linear region (linear approximation given by the red line) gives the built-in electrical potential φ_{bi} = 1.35 V.

Considering the capacitance due to the depletion region and minor charge carrier diffusion in alternating field in the forward biased region (negative potential applied to the top Ag electrode), the squared inverse capacitance density allows extracting the built-in electrical potential. In our case, the built-in potential was calculated to be φ_{bi} = 1.35 V and is rather high when compared to Si-based rectifying junctions.[37] In Figure 8c it can be observed that the major resistance nonlinearity does not coincide with the capacitance-voltage dependence, i.e. a sharp drop in resistance is observed in the low voltage range (0 V to -0.3 V), range in which the capacitance is

almost voltage-independent. This finding confirms that the depletion layer width modulation is not the main cause of the resistance change and of the existence of two distinct resistance states.

Conduction mechanism analysis. The characteristic conduction mechanism in the HRS and LRS states can be revealed by analyzing the derivative $\gamma = dLn(I)/dLn(V)$ as a function of the voltage, which corresponds to a straight line with an intercept of 0 or 1, for Schottky or Poole-Frenkel emission, respectively. Several conduction mechanisms show a γ ($V^{1/2}$) dependence e.g. for thermionic (Schottky) and Poole-Frenkel (PF) emission.[38] A constant γ value indicates possible Ohmic, Langmuir-Child or Space charge limited current (SCLC) conduction mechanisms (γ = 1, 1.5 and 2 respectively).

The Ag/GBCO/LNO memristors did not show rectifying behavior neither in the HRS nor in the LRS state, thus the Schottky emission mechanism could be discarded. The calculated $\gamma = dLn(I)/dLn(V)$ at room temperature for an Ag/GBCO/LNO memristor (layer thicknesses of 31 nm and 61 nm for GBCO and LNO, respectively) is displayed in Figure 9a.

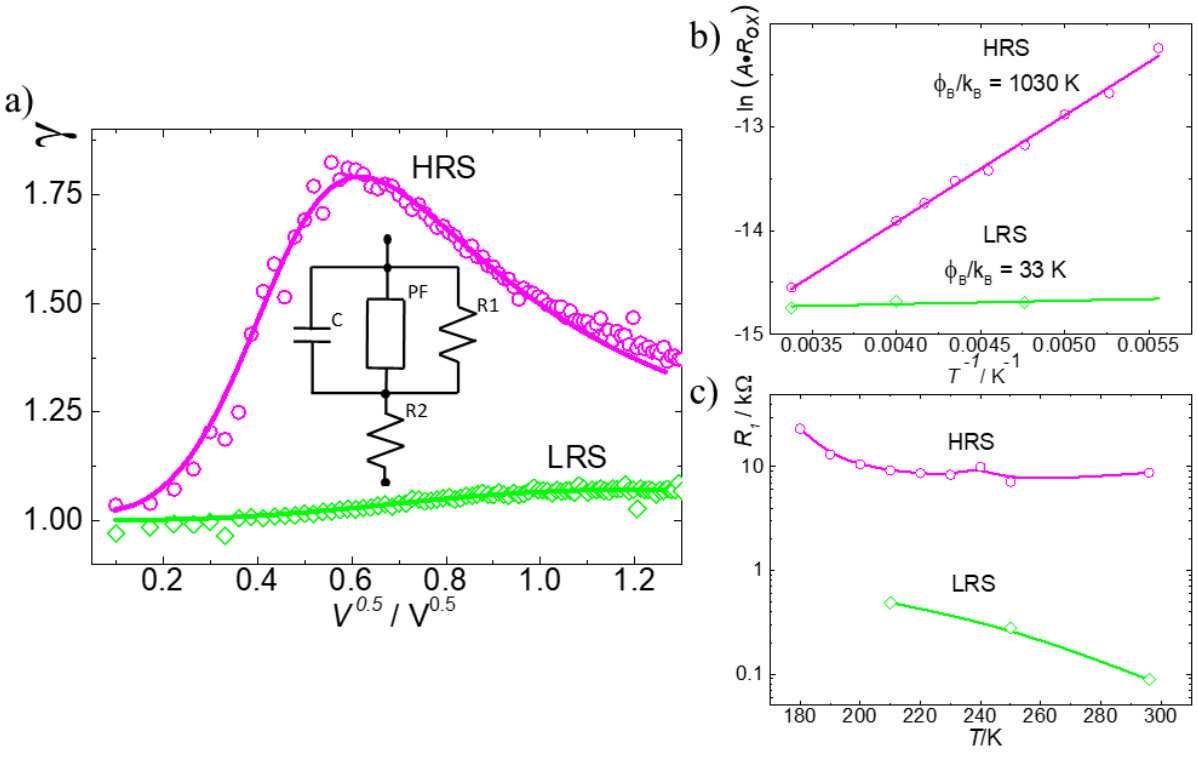

Figure 9. $\gamma(V^{1/2})$ dependence at room temperature a) the derivative calculated from the experimental data is shown for the HRS (purple circles) and LRS (green diamonds). The lines are the derivative of the experimental data fits by the Equation 2. The equivalent electrical circuit is shown in the inset. The semilogarithmic plot of $\ln(A \cdot R_{ox})$ vs. 1/T in b) allows extracting the barriers heights. c) R1 (fitting parameter) temperature dependence in HRS and LRS (the lines are guides for the eyes).

Clearly, the $\gamma(V^{1/2})$ dependence cannot be interpreted considering a single nonlinear element in the conduction pathway. In both resistance states γ is close to 1 at low voltages. In the HRS there is a voltage range (from 0.3 to 0.5 $V^{1/2}$) where γ increases linearly up to a maximum value of approximately 1.8 after which it gradually decreases to 1.3.

Such behavior can be modeled by the equivalent electrical circuit shown in the inset of Figure 9 a. The circuit consists of a non-linear element which is best described by the Poole-Frenkel emission conduction (also known as thermionic emission from the traps in a dielectric) and two resistances: R1 in parallel and R2 in series (the parallel capacitance is needed to account for the complex impedance frequency and bias dependence). The same equivalent circuit shown in the inset of Figure 9a, or a very similar one, had been previously used to describe the memristive behavior of other metal/perovskite oxide interfaces ([Au or Pt]/$YBa_2Cu_3O_7$[39] and $Ag/La_{0.325}Pr_{0.3}Ca_{0.375}MnO_3$[40]). The following formalism (also used in Acha *et al.*[41]) describes very well the experimentally observed I(V) curves and allows to extract the conduction mechanism and barriers heights in both HRS and LRS:

$$I = A(V - IR_2)exp\left[\frac{B(V-IR_2)^{\frac{1}{2}}}{k_B T}\right] + \frac{V-IR_2}{R_1}, \quad (2)$$

with

$$A = \frac{\exp\left(-\frac{\phi_B}{k_B T}\right)}{R_{ox}}, B = \frac{q^{3/2}}{(\pi\varepsilon' d)^{1/2}}, R_{ox} = \frac{d}{Sqn_0\mu}, \quad (3)$$

where T is absolute temperature, k_B is Boltzmann constant, Φ_B is a trap energy level, q is the elementary charge, S is the conducting area (equal to the top electrode area), ε' is the real part of the dielectric permittivity, n_0 and μ the charge carrier density and their mobility in the oxide layer respectively, and d is the oxide thickness.

Equation 2 is the rearranged form of the equation expressing the field dependence of the Poole-Frenkel emission from the traps in the oxide. The current induced by the externally applied voltage is distributed between the non-linear element and the parallel resistance; while the applied voltage is divided by the series resistor (geometrical resistance of the lower LNO electrode and LNO/GBCO/Pt). The derivatives calculated from the experimental I(V) curves in HRS and LRS match very well the derivatives of the experimental data fit by Equation 2. γ starts to deviate from the proposed circuit at high voltages (above 2 V), where another nonlinear process starts having a larger influence. Due to its very low contribution to the measured resistance, the precise nature of this element (additional resistance R1* in parallel to nonlinear PF element and R1) will not be thoroughly investigated in the present paper. Nevertheless, this element is linked to the conduction through the observed leaky capacitor C_p (Figure 7) and could be explained by direct or Fowler-Nordheim tunneling through the bipolar junction previously proposed.

The main contribution to the HRS/LRS ratio observed in Figure 3c and d comes from the modulation of the conductivity through the nonlinear PF element and parallel resistance R1 (Figure 9). The temperature dependence of the fitting parameter A/R_{ox} allowed extracting the trap energy levels in both states, which were found to be a 1030 K barrier height in HRS and almost no barrier in the LRS (33 K). The parallel resistance R1 qualitatively follows the temperature dependence

of the resistivity of an insulating GBCO phase ($\delta = 0.5$) for the HRS and of a conductive GBCO phase ($\delta > 0.5$) for the LRS.

Considering the structural and electrical characterization of the Ag/GBCO/LNO memristive heterostructures, we propose the following scenario to explain the observed resistive switching (schematic illustration shown in Figure 10).

Both GBCO and defective LNO (probably the mixture of $LaNiO_3$ and $La_2NiO_{4+\delta}$) are known for high oxygen mobility. They were developed as mixed electronic ionic conducting cathodes for intermediated temperature solid oxide fuel cells. Combined with Joule's heating allows consider that ionic oxygen can cross the bilayer interface and there is considerable oxygen exchange between constituents. Thus, even we have observed n-type conductivity by Hall measurement when GBCO was deposited directly on the $SrTiO_3$ substrate, it does not preclude the possibility to have oxygen rich, conductive GBCO when deposited on the LNO layer. Conductive GBCO ($\delta > 0.5$) perovskite acts as a p-type material (hole doped, paramagnetic metallic conduction[20]) and does not create a significant electron conduction barrier when in contact with p-type LNO (defective, oxygen hyper-stochiometric e.g. $La_2NiO_{4+\delta}$ behaves as a p-type semiconductor) and with relatively high work function metals such as Pt and Ag (Figure 10, bottom right). Accordingly, due to the conducting nature of hole-doped $GdBaCo_2O_{5+\delta}$ with a high oxygen content ($\delta > 0.5$) and to the absence of charge traps, we observe a very low barrier for the electron conduction in the GBCO film (bulk limited conduction mechanism, Poole-Frenkel barrier height of $\Phi_B = 33$ K). The lack of interface and bulk conduction barriers leads to the observed LRS state.

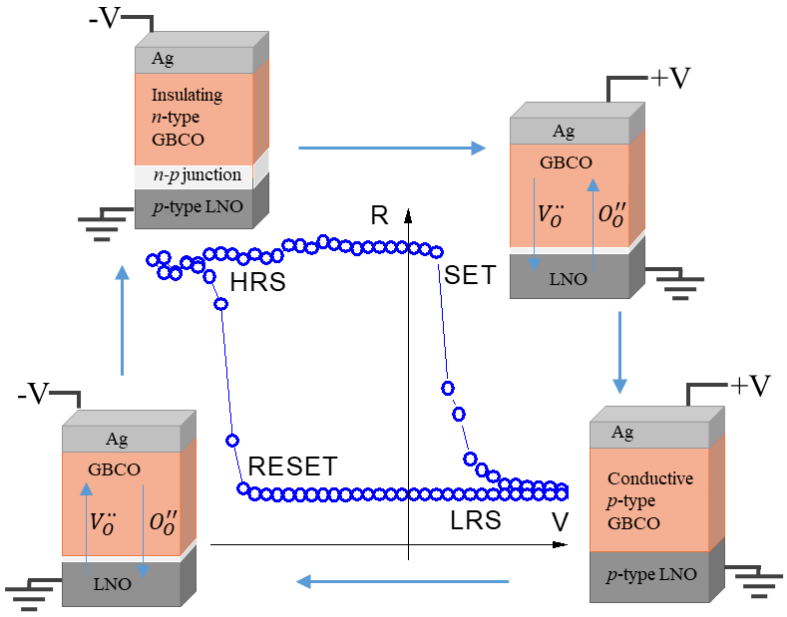

Figure 10. Schematic illustration of bi-mode interface and volume-type resistive switching between low (LRS) and high (HRS) resistance states.

When a negative voltage is applied to the top Ag electrode, positively charged oxygen vacancies drift along the electric field direction from the bottom LNO electrode into the GBCO layer towards the top Ag electrode (Figure 10, bottom left). Oxygen vacancy drift is expected from a combination of the applied field and Joule heating in the device. The decrease in oxygen content in the GBCO film influences the memristor's resistance in two ways: primarily increasing the GBCO resistance by creating charge traps which appear as a PF barrier with Φ_B = 1030 K, followed by the R1 parallel resistance increase by attracting oxygen vacancies and changing GBCO film into the insulating phase ($\delta \leq 0.5$ undoped or n doped phase diagram region[20]). The created n-p junction between n-type GBCO and p-type LNO layers hinders the oxygen ions back-diffusion (due to the oxygen concentration difference). These two phenomena, i.e. the increase of the bulk limited resistivity and the created electronic and ionic conduction barrier, lead to the observed highly nonlinear and non-volatile HRS state.

When the positive voltage is applied to the top Ag electrode, the oxygen vacancies are repelled from the GBCO layer into the LNO, increasing the GBCO conductivity by hole doping and eliminating the n-p junction by converting GBCO into a p-type semiconducting material. These mechanisms lead to a decrease of the overall resistance of the memristor and explain the observed LRS state.

CONCLUSIONS

We have shown that the mixed ionic-electronic conducting $GdBaCo_2O_{5+\delta}$ perovskite is an excellent active material for building non-filamentary resistive switching nanoionic devices. The observed memristive behavior in these devices can be explained by the superposition of volume and interface type resistive switching mechanisms in the $GdBaCo_2O_{5+\delta}$ /$LaNiO_3$ perovskite heterojunction.

Interestingly, the engineered Ag/GBCO/LNO memristive heterostructure presents two superimposed conduction limiting mechanisms, leading to non-volatile resistive switching. The first mechanism, responsible for the large memory window (up to 100 R_{HRS}/R_{LRS} ratio), is the variable bulk limited conduction (well described by an equivalent circuit with a non-linear Poole-Frenkel emission element). The second one, responsible for the non-volatility, is an electric field modulated non-homogeneous electron and anion conduction barrier created at the interface between dissimilar oxides (bipolar n-p junction at the GBCO/LNO interface). Such bi-modal resistive switching can be advantageous in other solid-state systems when creating switches from materials with high oxygen mobility.

AUTHOR INFORMATION

Corresponding Authors:

Dr. Sarunas Bagdzevicius email: sarunas.bagdzevicius@gmail.com.

Dr. Monica Burriel email: monica.burriel@grenoble-inp.fr.

AUTHOR CONTRIBUTIONS

S.B., J.M.C. and R.R-L. grew the films. S.B. performed the microstructural, electrical and electrochemical analysis and modelling and wrote the manuscript. Mi.Bo. helped with the supervision and discussion. L.R. carried out the TEM characterization and analysis. X.M. helped with the experimental electrical characterization. F.R. prepared the FIB lamellas. J.S. supervised the growth and characterization of the films and contributed to the discussion. Mo.Bu. conceived the original idea behind this study, supervised and co-wrote the manuscript. All authors have given approval to the final version of the manuscript.

Funding Sources

This work has been financed by the ANR funded project “MICROSWITCH” (ANR-14-ACHN-0012) and by the “FUN-TO-BE” CNRS-CSIC supported International Program for Scientific Cooperation (PICS, n°PICS07294). In addition, the work has been performed with the help of the “Plateforme Technologique Amont” of Grenoble, with the financial support of the “Nanosciences aux limites de la Nanoélectronique” Fundation and CNRS Renatech network, and has benefited from the facilities and expertise of the OPE)N(RA characterization platform of FMNT (FR 2542, fmnt.fr) supported by CNRS, Grenoble INP and UGA.

ACKNOWLEDGMENT

Dr. Hervé Roussel from LMGP, Grenoble, France is acknowledged for XRD analysis.

REFERENCES

(1) Waldrop, M. M. More than Moore. *Nature* **2016**, *530* (7589), 144–147.

(2) Semiconductor Industry Association. *International Technology Roadmap for Semiconductors 2.0 2015 Edition, Beyond CMOS*; 2015.

(3) Lee, J. S.; Lee, S.; Noh, T. W. Resistive Switching Phenomena: A Review of Statistical Physics Approaches. *Appl. Phys. Rev.* **2015**, *2* (3), 031303.

(4) Yang, J. J.; Strukov, D. B.; Stewart, D. R. Memristive Devices for Computing. *Nat. Nanotechnol.* **2012**, *8* (1), 13–24.

(5) Sharath, S. U.; Vogel, S.; Molina-Luna, L.; Hildebrandt, E.; Wenger, C.; Kurian, J.; Duerrschnabel, M.; Niermann, T.; Niu, G.; Calka, P.; et al. Control of Switching Modes and Conductance Quantization in Oxygen Engineered HfO x Based Memristive Devices. *Adv. Funct. Mater.* **2017**, *27* (32), 1700432.

(6) Kuzum, D.; Yu, S.; Wong, H.-S. P. S. Synaptic Electronics: Materials, Devices and Applications. *Nanotechnology* **2013**, *24* (38), 382001.

(7) A. Sawa, R. M.; Sawa, A.; Meyer, R. Interface-Type Switching. In *Resistive Switching: From Fundamentals of Nanoionic Redox Processes to Memristive Device Applications*; Wiley-VCH Verlag GmbH & Co. KGaA: Weinheim, Germany, Germany, 2016; pp 457–482.

(8) Stoliar, P.; Levy, P.; Sanchez, M. J.; Leyva, A. G.; Albornoz, C. A.; Gomez-Marlasca, F.; Zanini, A.; Toro Salazar, C.; Ghenzi, N.; Rozenberg, M. J. Nonvolatile Multilevel Resistive Switching Memory Cell: A Transition Metal Oxide-Based Circuit. *IEEE Trans. Circuits Syst. II Express Briefs* **2014**, *61* (1), 21–25.

(9) Park, S.; Kim, H.; Choo, M.; Noh, J.; Sheri, A.; Jung, S.; Seo, K.; Park, J.; Kim, S.; Lee,

W.; et al. RRAM-Based Synapse for Neuromorphic System with Pattern Recognition Function. In *2012 International Electron Devices Meeting*; IEEE, 2012; p 10.2.1-10.2.4.

(10) Bagdzevicius, S.; Maas, K.; Boudard, M.; Burriel, M. Interface-Type Resistive Switching in Perovskite Materials. *J. Electroceramics* **2017**, *39* (April), 1–28.

(11) Vitale, W. A.; Casu, E. A.; Biswas, A.; Rosca, T.; Alper, C.; Krammer, A.; Luong, G. V.; Zhao, Q.-T.; Mantl, S.; Schüler, A.; et al. A Steep-Slope Transistor Combining Phase-Change and Band-to-Band-Tunneling to Achieve a Sub-Unity Body Factor. *Sci. Rep.* **2017**, *7* (1), 355.

(12) Janod, E.; Tranchant, J.; Corraze, B.; Querré, M.; Stoliar, P.; Rozenberg, M.; Cren, T.; Roditchev, D.; Phuoc, V. T.; Besland, M.-P.; et al. Resistive Switching in Mott Insulators and Correlated Systems. *Adv. Funct. Mater.* **2015**, *25* (40), 6287–6305.

(13) Lee, H. S.; Choi, S. G.; Park, H. H.; Rozenberg, M. J. A New Route to the Mott-Hubbard Metal-Insulator Transition: Strong Correlations Effects in Pr0.7Ca0.3MnO3. *Sci. Rep.* **2013**, *3*, 1–5.

(14) Gonzalez-Rosillo, J. C.; Ortega-Hernandez, R.; Jareño-Cerulla, J.; Miranda, E.; Suñe, J.; Granados, X.; Obradors, X.; Palau, A.; Puig, T. Volume Resistive Switching in Metallic Perovskite Oxides Driven by the Metal-Insulator Transition. *J. Electroceramics* **2017**, *39* (1–4), 185–196.

(15) Palau, A.; Fernandez-Rodriguez, A.; Gonzalez-Rosillo, J. C.; Granados, X.; Coll, M.; Bozzo, B.; Ortega-Hernandez, R.; Suñé, J.; Mestres, N.; Obradors, X.; et al. Electrochemical Tuning of Metal Insulator Transition and Nonvolatile Resistive Switching in Superconducting Films. *ACS Appl. Mater. Interfaces* **2018**, *10* (36), 30522–30531.

(16) Schmitt, R.; Spring, J.; Korobko, R.; Rupp, J. L. M. Design of Oxygen Vacancy

Configuration for Memristive Systems. *ACS Nano* **2017**, *11* (9), 8881–8891.

(17) Ortega-Hernandez, R.; Coll, M.; Gonzalez-Rosillo, J.; Palau, A.; Obradors, X.; Miranda, E.; Puig, T.; Suñe, J. Resistive Switching in CeO2/La0.8Sr0.2MnO3 Bilayer for Non-Volatile Memory Applications. *Microelectron. Eng.* **2015**, *147*, 37–40.

(18) Zhu, Y.; Li, M.; Liu, J.; Hu, Z.; Wang, Q.; Zhang, Y.; Wei, M.; Hu, C. Resistive Switching Behavior in Pt/YSZ/Nb:SrTiO3 Heterostructure for Nonvolatile Multilevel Memories. *J. Alloys Compd.* **2014**, *612*, 30–33.

(19) Arndt, B.; Borgatti, F.; Offi, F.; Phillips, M.; Parreira, P.; Meiners, T.; Menzel, S.; Skaja, K.; Panaccione, G.; MacLaren, D. A.; et al. Spectroscopic Indications of Tunnel Barrier Charging as the Switching Mechanism in Memristive Devices. *Adv. Funct. Mater.* **2017**, *27* (45), 1702282.

(20) Taskin, A. A.; Lavrov, A. N.; Ando, Y. Transport and Magnetic Properties of GdBaCo2O5+x Single Crystals: A Cobalt Oxide with Square-Lattice CoO2 Planes over a Wide Range of Electron and Hole Doping. *Phys. Rev. B* **2005**, *71* (13), 134414.

(21) Zapata, J.; Burriel, M.; García, P.; Kilner, J. A.; Santiso, J. Anisotropic 18O Tracer Diffusion in Epitaxial Films of GdBaCo2O5+δ Cathode Material with Different Orientations. *J. Mater. Chem. A* **2013**, *1* (25), 7408.

(22) Burriel, M.; Casas-Cabanas, M.; Zapata, J.; Tan, H.; Verbeeck, J.; Solís, C.; Roqueta, J.; Skinner, S. J.; Kilner, J. a.; Van Tendeloo, G.; et al. Influence of the Microstructure on the High-Temperature Transport Properties of GdBaCo 2 O 5.5+δ Epitaxial Films. *Chem. Mater.* **2010**, *22* (19), 5512–5520.

(23) Correa, J. A. Z. *Epitaxial Thin Film Growth and Study of Charge and Mass Transport Properties of Mixed Ionic Electronic Conducting GdBaCo2O5+δ (GBCO)*;

https://ddd.uab.cat/record/165243, 2016.

(24) Frontera, C.; García-Muñoz, J. L.; Llobet, A.; Aranda, M. a. G. Selective Spin-State Switch and Metal-Insulator Transition in GdBaCo2O5.5. *Phys. Rev. B* **2002**, *65* (18), 180405.

(25) Roy, S.; Khan, M.; Guo, Y. Q.; Craig, J.; Ali, N. Observation of Low, Intermediate, and High Spin States in GdBaCo2O5.45. *Phys. Rev. B* **2002**, *65* (6), 064437.

(26) Coll, C.; López-Conesa, L.; Rebled, J. M.; Magén, C.; Sánchez, F.; Fontcuberta, J.; Estradé, S.; Peiró, F. Simulation of STEM-HAADF Image Contrast of Ruddlesden–Popper Faulted LaNiO 3 Thin Films. *J. Phys. Chem. C* **2017**, *121* (17), 9300–9304.

(27) Son, J.; Moetakef, P.; LeBeau, J. M.; Ouellette, D.; Balents, L.; Allen, S. J.; Stemmer, S. Low-Dimensional Mott Material: Transport in Ultrathin Epitaxial LaNiO3 Films. *Appl. Phys. Lett.* **2010**, *96* (6), 062114.

(28) Jorgensen, J. D.; Dabrowski, B.; Pei, S.; Richards, D. R.; Hinks, D. G. Structure of the Interstitial Oxygen Defect in La2NiO4+δ. *Phys. Rev. B* **1989**, *40* (4), 2187–2199.

(29) Chen, A. B. K.; Choi, B. J.; Yang, X.; Chen, I.-W. A Parallel Circuit Model for Multi-State Resistive-Switching Random Access Memory. *Adv. Funct. Mater.* **2012**, *22* (3), 546–554.

(30) Mikheev, E.; Hoskins, B. D.; Strukov, D. B.; Stemmer, S. Resistive Switching and Its Suppression in Pt/Nb:SrTiO3 Junctions. *Nat. Commun.* **2014**, *5*, 3990.

(31) Yang, C.-H.; Seidel, J.; Kim, S. Y.; Rossen, P. B.; Yu, P.; Gajek, M.; Chu, Y. H.; Martin, L. W.; Holcomb, M. B.; He, Q.; et al. Electric Modulation of Conduction in Multiferroic Ca-Doped BiFeO3 Films. *Nat. Mater.* **2009**, *8* (6), 485–493.

(32) Nomerovannaya, L. V.; Makhnev, A. A.; Naumov, S. V.; Telegin, S. V. Optical Properties and Electronic Structure of Cobalt-Deficit GdBaCo1.86O5 + δ Single Crystals. *Phys. Solid State* **2015**, *57* (4), 776–780.

(33) E.H. Rhoderick. Metal-Semiconductor Contacts. *Phys. Technol.* **1974**, *5* (4), 223–223.

(34) Lucia, M. L.; Hernandez-Rojas, J. L.; Leon, C.; Mártil, I. Capacitance Measurements of P-n Junctions: Depletion Layer and Diffusion Capacitance Contributions. *Eur. J. Phys.* **1993**, *14* (2), 86–89.

(35) Tsipis, E. V.; Naumovich, E. N.; Shaula, A. L.; Patrakeev, M. V.; Waerenborgh, J. C.; Kharton, V. V. Oxygen Nonstoichiometry and Ionic Transport in La2Ni(Fe)O4 + δ. *Solid State Ionics* **2008**, *179* (1–6), 57–60.

(36) Scherwitzl, R.; Zubko, P.; Lichtensteiger, C.; Triscone, J. M. Electric-Field Tuning of the Metal-Insulator Transition in Ultrathin Films of LaNiO3. *Appl. Phys. Lett.* **2009**, *95* (22), 1–4.

(37) Tung, R. T. The Physics and Chemistry of the Schottky Barrier Height. *Appl. Phys. Rev.* **2014**, *1* (1).

(38) Lim, E.; Ismail, R. Conduction Mechanism of Valence Change Resistive Switching Memory: A Survey. *Electronics* **2015**, *4* (3), 586–613.

(39) Acha, C. Dynamical Behaviour of the Resistive Switching in Ceramic YBCO/Metal Interfaces. *J. Phys. D. Appl. Phys.* **2011**, *44* (34), 345301.

(40) Gomez-Marlasca, F.; Ghenzi, N.; Leyva, A. G.; Albornoz, C.; Rubi, D.; Stoliar, P.; Levy, P. Modeling Electronic Transport Mechanisms in Metal-Manganite Memristive Interfaces. *J. Appl. Phys.* **2013**, *113* (14), 144510.

(41) Acha, C.; Schulman, A.; Boudard, M.; Daoudi, K.; Tsuchiya, T. Transport Mechanism through Metal-Cobaltite Interfaces. *Appl. Phys. Lett.* **2016**, *109* (1), 011603.

Graphical Table of Contents